Author/s:
Nguyen, CK;Mazumder, A;Mayes, ELH;Krishnamurthi, V;Zavabeti, A;Murdoch, BJ;Guo, X;Aukarasereenont, P;Dubey, A;Jannat, A;Wei, X;Truong, VK;Bao, L;Roberts, A;McConville, CF;Walia, S;Syed, N;Daeneke, T

Title:
2-nm-Thick Indium Oxide Featuring High Mobility

Date:
2023-03-24

Citation:
Nguyen, C. K., Mazumder, A., Mayes, E. L. H., Krishnamurthi, V., Zavabeti, A., Murdoch, B. J., Guo, X., Aukarasereenont, P., Dubey, A., Jannat, A., Wei, X., Truong, V. K., Bao, L., Roberts, A., McConville, C. F., Walia, S., Syed, N. & Daeneke, T. (2023). 2-nm-Thick Indium Oxide Featuring High Mobility. Advanced Materials Interfaces, 10 (9), https://doi.org/10.1002/admi.202202036.

Persistent Link:
https://hdl.handle.net/11343/328283

ADVANCED MATERIALS INTERFACES
Open Access
www.advmatinterfaces.de

2-nm-Thick Indium Oxide Featuring High Mobility

Chung Kim Nguyen, Aishani Mazumder, Edwin LH Mayes, Vaishnavi Krishnamurthi, Ali Zavabeti, Billy J. Murdoch, Xiangyang Guo, Patjaree Aukarasereenont, Aditya Dubey, Azmira Jannat, Xiaotian Wei, Vi Khanh Truong, Lei Bao, Ann Roberts, Chris F. McConville, Sumeet Walia, Nitu Syed, and Torben Daeneke**

Thin film transistors (TFTs) are key components for the fabrication of electronic and optoelectronic devices, resulting in a push for the wider exploration of semiconducting materials and cost-effective synthesis processes. In this report, a simple approach is proposed to achieve 2-nm-thick indium oxide nanosheets from liquid metal surfaces by employing a squeeze printing technique and thermal annealing at 250 °C in air. The resulting materials exhibit a high degree of transparency (>99 %) and an excellent electron mobility of ≈96 $cm^2 V^{-1} s^{-1}$, surpassing that of pristine printed 2D In_2O_3 and many other reported 2D semiconductors. UV-detectors based on annealed 2D In_2O_3 also benefit from this process step, with the photoresponsivity reaching 5.2×10^4 and 9.4×10^3 A W^{-1} at the wavelengths of 285 and 365 nm, respectively. These values are an order of magnitude higher than for as-synthesized 2D In_2O_3. Utilizing transmission electron microscopy with in situ annealing, it is demonstrated that the improvement in device performances is due to nanostructural changes within the oxide layers during annealing process. This work highlights a facile and ambient air compatible method for fabricating high-quality semiconducting oxides, which will find application in emerging transparent electronics and optoelectronics.

1. Introduction

2D semiconducting materials have been intensively investigated and recognized as promising candidates for the next generation thin film electronics.[1] In particular, 2D metal oxides (2D MOXs) represent an exciting class of 2D semiconducting materials and have attracted considerable interest due to their wide bandgaps, high carrier mobility, and good environmental stability.[1c,2] However, the controlled synthesis of high-quality 2D oxide films across large areas, required to enable the development of highly integrated devices, remains a significant challenge that needs to be resolved prior to industrial and commercial applications of such emerging materials.[1b,c]

To this end, liquid metal-based printing methods have recently been developed, offering an appealing approach for the facile, cost-effective,

C. K. Nguyen, A. Mazumder, V. Krishnamurthi, X. Guo, A. Dubey, X. Wei, L. Bao, S. Walia, N. Syed, T. Daeneke
School of Engineering
RMIT University
Melbourne, VIC 3001, Australia
E-mail: nitu.syed@unimelb.edu.au; torben.daeneke@rmit.edu.au

E. L. Mayes, B. J. Murdoch
RMIT Microscopy and Microanalysis Facility
College of Science
Engineering & Health
RMIT University
Melbourne, VIC 3001, Australia

A. Zavabeti, P. Aukarasereenont, C. F. McConville
School of Science
RMIT University
Melbourne, VIC 3001, Australia

A. Zavabeti
Department of Chemical Engineering
The University of Melbourne
Parkville, VIC 3010, Australia

A. Jannat
Research School of Physics
The Australian National University
Canberra, ACT 2601, Australia

V. K. Truong
College of Medicine and Public Health
Flinders University
Bedford Park, SA 5042, Australia

A. Roberts, N. Syed
ARC Centre of Excellence for Transformative Meta-Optical Systems
School of Physics
The University of Melbourne
Parkville, VIC 3010, Australia

C. F. McConville
Institute for Frontier Materials
Deakin University
Waurn Ponds, Geelong, VIC 3216, Australia

The ORCID identification number(s) for the author(s) of this article can be found under https://doi.org/10.1002/admi.202202036.

DOI: 10.1002/admi.202202036

and relatively low-temperature synthesis of 2D MOXs.[2b,3] These techniques rely on the Cabrera–Mott oxidation of metals, which results in the formation of an atomically thin and self-passivating oxide skin across the metal surface.[4] Due to the nature of the parent liquid metal, the interfacial oxide layer exhibits weak adhesion to the host metal and can readily be transferred to target substrates with minimal imperfections.[3a,b,4b] This simple approach can be utilized to produce 2D nanosheets of both stratified and unstratified metal oxides, which is challenging with conventional exfoliation processes.[3a–c]

In comparison to vapor phase deposition techniques, liquid metal printing is straightforward and can be conducted in ambient atmosphere.[2b,3d,5] The synthesized 2D oxide films can reach wafer scale while retaining their ultrathin nature, high uniformity, and excellent electronic characteristics, demonstrating the promise for vacuum-free 2D MOXs deposition.[5a–d] Moreover, with thicknesses down to 1–2 nm, 2D MOXs deposited from liquid metals feature excellent transparency (>98%) and mechanical flexibility, making them promising candidates for transparent and flexible thin film transistors (TFTs).[5b,c,f]

Among several 2D MOXs, indium oxide is an important n-type semiconductor due to its high electron mobility (≈160 $cm^2\ V^{-1}\ s^{-1}$ for single crystals), tuneable electrical properties, and excellent optical transparency.[2a,6] Recent efforts to realize ultrathin In_2O_3 from molten indium metal have also been reported.[5a,c,f,7] However, as-synthesized 2D In_2O_3 nanosheets featured a low carrier mobility of only ≈5 $cm^2\ V^{-1}\ s^{-1}$,[5c,f,7] providing plenty of room for further improvement.

Herein, we utilize the liquid metal printing technique to prepare ultrathin and large-area In_2O_3 nanosheets. The effects of low-temperature annealing on the crystal structure and electronic properties of these materials are then investigated. We demonstrate that a simple postsynthesis annealing process at 250 °C results in improved uniformity and larger grain sizes, while also reducing disorder at the grain boundaries, boosting the performance of field effect transistors (FETs) and solar-blind UV detectors. The observed carrier mobility approaches that of single crystal In_2O_3, highlighting an exciting pathway towards the next generation of miniaturized electronic and optoelectronic circuits.

2. Results and Discussion

A schematic of 2D In_2O_3 nanosheets synthesized by employing the liquid metal printing technique is shown in **Figure 1**a,b. The synthesis was carried out in an ambient atmosphere. The ultrathin oxide layers grow spontaneously on the surface of molten indium metal and are then transferred to the desired substrate by squeeze printing (see the Experimental Section for the detailed synthesis process). Continuous 2D nanosheets deposited on SiO_2/Si substrates approaching millimeter scale are routinely achieved and can be seen in Figure 1c and Figure S1 in the Supporting Information. It should be noted that larger amounts of molten metal can be used to readily increase the lateral dimension of 2D In_2O_3 nanosheets.[5c,f] Furthermore, a continuous printing process has recently been developed, demonstrating that wafer scale deposition via liquid metal processing is quite feasible.[5d]

To explore the electron transport properties of the produced 2D oxide nanosheets, back-gated field-effect transistors (FETs) were fabricated using 2D In_2O_3 as the semiconducting channels (**Figure 2**a, inset). The performance of a non-annealed 2D In_2O_3 FET has been shown in Figure S2, Supporting Information, featuring a mobility of 7 $cm^2\ V^{-1}\ s^{-1}$ and an on/off ratio of 10^2. Upon annealing at 250 °C for 2 h in ambient air, the FET performances were remarkably improved. Figure 2a,b presents the output curves ($I_{DS} - V_{DS}$) and transfer curves ($I_{DS} - V_{GS}$) of the produced transistors based on annealed 2D In_2O_3 nanosheets. This indicates n-channel semiconducting behavior with an excellent carrier mobility of ≈96 $cm^2\ V^{-1}\ s^{-1}$, which is comparable to the reported value for polycrystalline-silicon TFTs (50–100 $cm^2\ V^{-1}\ s^{-1}$).[8] In addition, the transistors based on annealed 2D In_2O_3 exhibited a considerable on/off current ratio of ≈10^4 with a clear depletion mode observed at V_{GS} = –40 V (Figure 2c). It is important to note that the on/off ratio can be further improved by optimizing the dielectric layer or engineering the device architecture.[3d,9] Figure 2d illustrates the mobility statistics, demonstrating the highly consistent performance of these FET devices. The optimized annealing condition was identified to be 250 °C for a duration of 2 h, which led to the FET mobility of 95.7 ± 4.8 $cm^2\ V^{-1}\ s^{-1}$. Herein, the maximum temperature of the whole annealing process was limited to 250 °C, which enables device fabrication on flexible

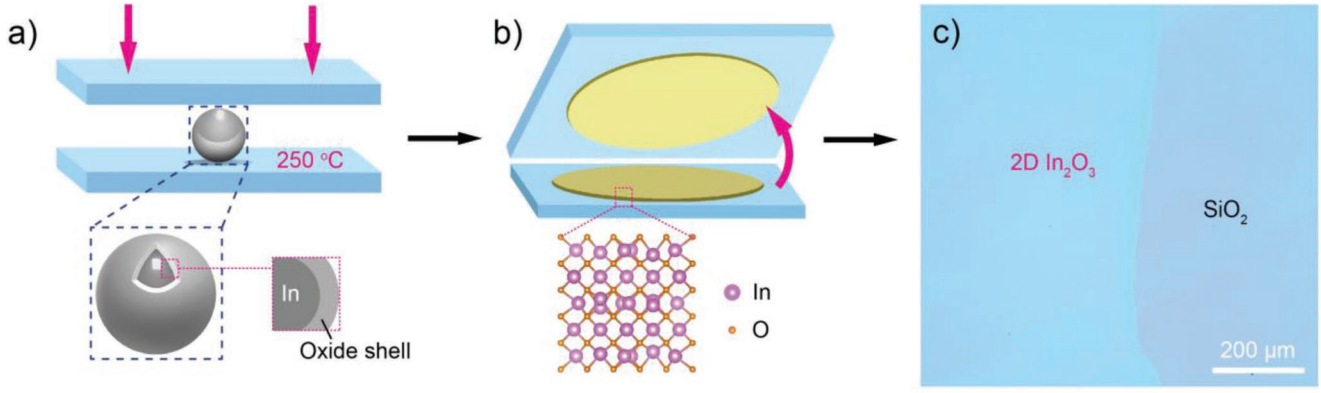

Figure 1. a,b) Schematic illustration of the squeeze printing technique for the synthesis of ultrathin indium oxide. c) Optical image of 2D In_2O_3 prepared on SiO_2 (300 nm)/Si substrate.

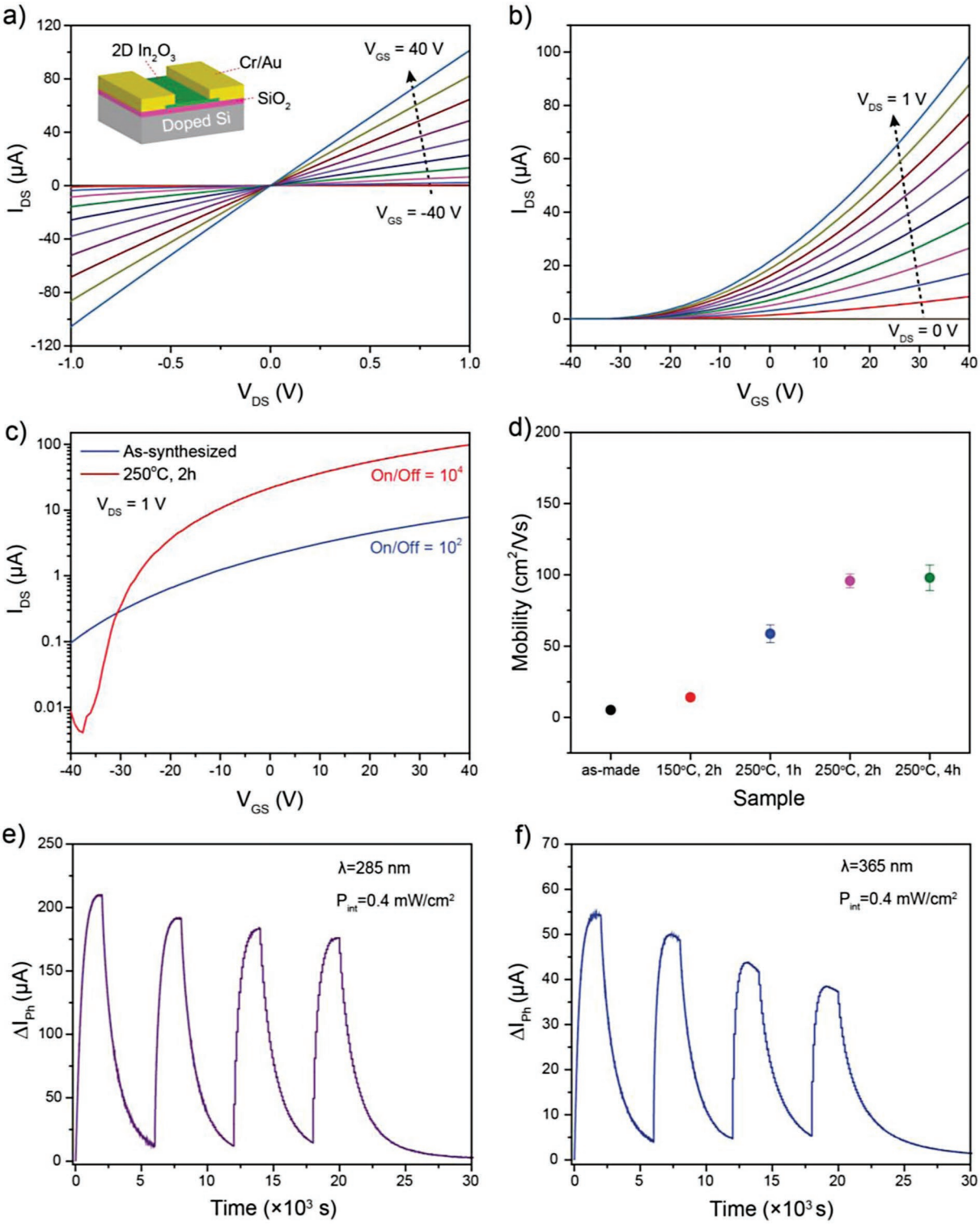

Figure 2. Electronic and optoelectronic performance of the 2D In_2O_3 nanosheets. a,b) FET performance of a device based on annealed 2D In_2O_3. The inset in (a) shows the schematic structure of the device. a) Output curves when V_{GS} varies from –40 to 40 V. b) Transfer curves with V_{DS} ranging from 0 to 1 V. c) The I_{DS}–V_{GS} data in semi-log scale at V_{DS} = 1 V with on/off ratios. d) Carrier mobility of 2D In_2O_3 nanosheets at different anneal conditions. These mobility data were collected from 15 devices and shown in average values with standard errors. e,f) On/off switching photocurrent cycles of a photodetector based on annealed In_2O_3 measured at e) 285 nm and f) 365 nm UV exposure with a power intensity of 0.4 mW cm^{-2} and a bias voltage of 0.5 V.

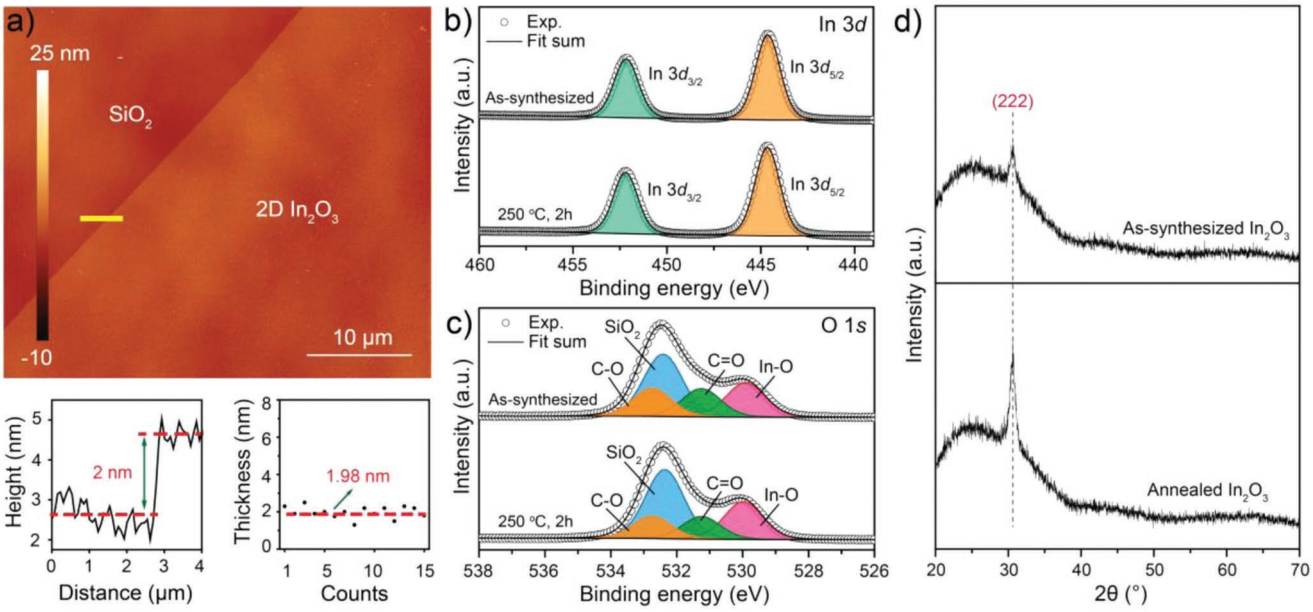

Figure 3. a) AFM image of an annealed 2D In_2O_3 nanosheet with the corresponding step height profile (lower left inset) and thickness analysis of 15 edge locations collected from 5 separate nanosheets (lower right inset). The average thickness with the standard error was calculated to be 1.98 ± 0.08 nm. b,c) XPS spectra in the In 3d and O 1s regions of the fresh and annealed 2D In_2O_3 nanosheets prepared on 300 nm SiO_2/Si substrate. d) XRD patterns of as-synthesized and annealed 2D In_2O_3 multiple-printed on glass substrates. Annealing was performed at 250 °C for 2 h in air.

substrates such as polydimethylsiloxane (PDMS) and polyimides (e.g., Kapton).[5b,10] Addition FET performances can be found in Figure S3 in the Supporting Information.

Taking advantage of the wide bandgap of 2D In_2O_3 (E_g^{opt} = ≈3.7 eV), we have recently demonstrated the use of few-nm-thick In_2O_3 for optoelectronic applications in the UV region.[5c] Several works have reported that a photodetector's performance can be enhanced by annealing,[11] and here we investigate annealed 2D In_2O_3 nanosheet based photodetectors. The optoelectronic properties of annealed 2D In_2O_3 nanosheets were investigated by irradiating two-terminal planar devices (Figure 2a, inset) with light sources of 285 and 365 nm. The UV detection performances were then compared with published data for UV-detectors based on as-exfoliated 2D In_2O_3 nanosheets (Table S1, Supporting Information).

As shown in Figure 2e,f, and Table S1, Supporting Information, annealing 2D-In_2O_3 nanosheets at 250 °C in air for 2 h likely reduced the recombination rate of electron-hole pairs, which ultimately increased the photocurrent multifold.[12] This finding suggests that the annealing process reduced defects in the In_2O_3 layer which can act as recombination sites, and improved charge carrier extraction due to improved mobility resulting in larger carrier diffusion length.[13] Besides the improved photocurrent, the annealing also facilitated in enhancing the figures of merit (FoM) for all three parameters of responsivity (R), detectivity (D^*), and external quantum efficiency (EQE), which were an order of magnitude higher after annealing when compared with pristine In_2O_3, thereby showing superior performance (Table S1, Supporting Information).

Comprehensive materials characterization has been conducted to further clarify the role of thermal annealing in boosting carrier mobility. It is well established that the electronic and optical properties of 2D materials are typically thickness dependent,[1c,14] and inconsistencies in the performance of electronic devices are often caused by non-uniform thicknesses and defects created during the deposition process.[1c] Therefore, atomic force microscopy (AFM) has been used to assess the uniformity and surface morphology of isolated 2D In_2O_3 nanosheets. From AFM data, no obvious changes in film thickness were observed after annealing. Both freshly deposited and annealed samples featured atomically flat and uniform 2D sheets covering large areas with minimal cracks, folds, and pinholes (**Figure 3**a; Figure S4a, Supporting Information). Analysis of 15 edge locations indicated that liquid metal printing is highly reproducible with an average thickness of 1.98 ± 0.08 nm for annealed 2D In_2O_3 (Figure 3a, lower right inset and Figure S4b in the Supporting Information), which is similar to the thickness of as-exfoliated 2D In_2O_3 reported in our recent work (2.08 ± 0.07 nm)[5c] and matches well with two unit cells of cubic In_2O_3 (a = 10.12 Å).[15] Due to their atomically thin nature, 2D In_2O_3 nanosheets offer an ultra-high transparency across the visible and near-infrared regions (Figure S5, Supporting Information). The as-synthesized and annealed 2D In_2O_3 nanosheets exhibited a transmittance of 98.5% and 99.6% at the wavelength 550 nm, respectively, clearly demonstrating that annealing improves the optical properties of the 2D In_2O_3 nanosheets. The optical absorption of pristine In_2O_3 is comparable, while that of annealed samples is superior to the 97.4% optical transmittance of monolayer graphene.[16]

The chemical composition of the as-synthesized and annealed 2D In_2O_3 nanosheets was determined by X-ray photoelectron spectroscopy (XPS), with the spectra of In 3d and O 1s presented in Figure 3b,c. The characteristic doublets of In $3d_{5/2}$ and In $3d_{3/2}$ can be observed at ≈444.6 and ≈452.2 eV, respectively, identifying the +3 oxidation state of indium in the 2D oxide sheets (Figure 3b).[5b,17] Figure 3c shows O 1s spectra

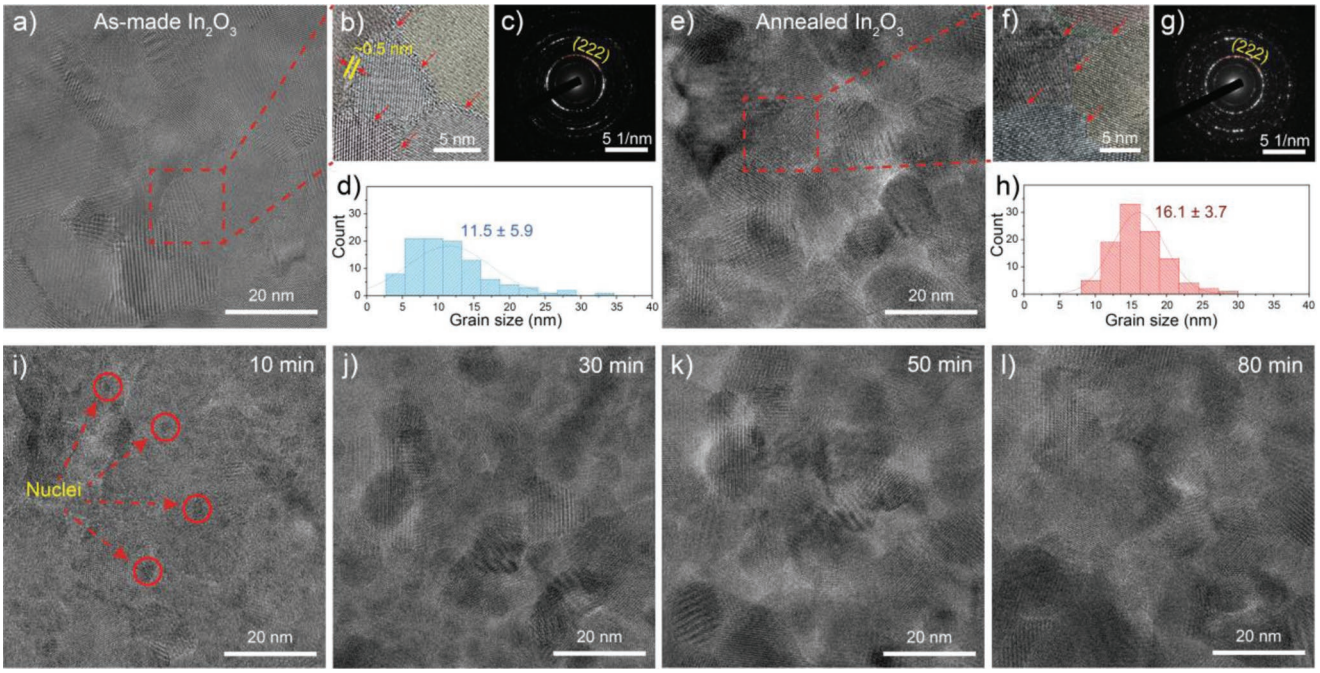

Figure 4. a–h) HRTEM images with corresponding zoom-in areas, SAED patterns, and grain size distributions of a–d) pristine and e–h) annealed 2D In_2O_3 nanosheets. Color-coded areas in (b) and (f) represent the crystal grains with red arrows indicating the grain boundaries. i–l) In situ TEM of 2D In_2O_3 nanosheets at 250 °C indicating the recrystallization of 2D In_2O_3. The nucleation sites were indicated in (i) and the growth of crystal grains can be observed during the thermal annealing. All TEM images were taken from the same 2D In_2O_3 nanosheet.

which contain peaks associated with various oxygen species. The peak at ≈529.9 eV pertains to oxygen bound to indium, whilst the remainder are related to either the oxide layer on the Si/SiO_2 substrate (≈532.4 eV) or to residual organic contaminants (≈531.3 and ≈532.8 eV for C=O and C—O, respectively). No change to the oxidation state was observed after annealing. The only variation in the O 1*s* spectrum observed after annealing was a small reduction in the contaminant peaks. This was accompanied by a 10% reduction in the total C 1s signal relative to In 3d.

Optical characterization of the nonannealed and annealed 2D In_2O_3 nanosheets was used to investigate possible changes in the band structure of 2D oxide nanosheets due to thermal annealing. Tauc plot analysis revealed an optical bandgap of ≈3.6 eV for the annealed 2D In_2O_3, which is slightly lower than the ≈3.7 eV measured for as-exfoliated samples (Figure S6, Supporting Information), indicating that if any changes to the electronic band structure occurred, they were likely minimal.

Repeated printing resulting in the deposition of thicker films enabled the collection of X-ray diffraction (XRD) patterns which are displayed in Figure 3d. The XRD patterns reveal the crystal structure of 2D In_2O_3 nanosheets synthesized from liquid metal. The peak at ≈30.6° can be attributed to the (222) plane of cubic indium oxide[15] with the intensity increasing significantly upon annealing the sample. As such, annealing was found to not change the crystallization habit of cubic In_2O_3, but instead to increase the overall crystallinity of the deposited material, hence improving the electronic properties of the 2D In_2O_3 nanosheets. Nevertheless, XRD in of itself does not provide sufficient evidence to identify the precise nanostructural changes that occur within the 2D materials upon thermal treatment. Therefore, transmission electron microscopy (TEM) with in situ heating was performed at 250 °C to study the microscopic changes in detail and gain further insight into modifications to the crystal structure and transformation of 2D In_2O_3 nanosheets during annealing (**Figure 4**). This technique allows real-time observation of structural evolution at the atomic scale during the thermal annealing process, and Video S1 in the Supporting Information showcases a time-lapse of the two-hour-annealing process.

In contrast to a recent study reporting an amorphous-crystalline heterophase of 2D In_2O_3 printed from liquid metal at a lower temperature of 165 °C,[5a] our work demonstrates that printing at a higher temperature (i.e., 250 °C) directly results in polycrystalline 2D In_2O_3 nanosheets (Figure 4a). Interestingly, many nanocrystals within the as-printed nanosheet were found to be surrounded by an approximate 0.5 nm thick distorted boundary region (Figure 4b). After 10 min of annealing (Figure 4i), several additional nucleation sites appeared and grew throughout the annealing process, resulting in the partial recrystallization of the 2D oxide film (Figure 4i–l).

As shown in Figure 4a–h, the crystallographic structure of 2D In_2O_3 nanosheets significantly changed after annealing. It is clear from the grain size distributions shown in Figure 4d, h that the crystal domain size increased from 11.5 ± 5.9 to 16.1 ± 3.7 nm after annealing at 250 °C for 2 h. This finding explains the origin of increased carrier mobility of annealed 2D In_2O_3 in part, as the increase in crystal domain sizes results in fewer grain boundaries, and hence fewer charge transport barriers.[1c,18] More importantly, the intergranular distorted regions, which may present significant potential barriers to charge transport, were evident in the as-made 2D In_2O_3

(Figure 4b). As grains ripened during annealing, these regions were absorbed by the growing crystalline domains (Figure 4f), contributing to the observed increase in carrier mobility. Additional TEM images of 2D In_2O_3 can be seen in Figure S7 in the Supporting Information.

Interestingly, the selected area electron diffraction (SAED) pattern shown in Figure 4c reveals a partially aligned crystal structure for the pristine 2D In_2O_3, in which the (222) diffraction spots appear in clusters and are thus preferentially oriented. In contrast, the annealed nanosheets exhibited a random crystal orientation with diffraction spots forming a ring without significant clustering (Figure 4g). Here, it should be noted that from the viewpoints of TFT device fabrication, randomly oriented nanocrystalline 2D semiconductors are preferred over highly oriented ones, since it minimizes the effect of anisotropic carrier mobilities along a material's crystal axes. This finding highlights the potential of implementing a thermal annealing process for practical applications of liquid metal derived 2D In_2O_3 nanosheets.

3. Conclusions

In this work, we have demonstrated a scalable method for synthesizing large-area and ultrathin In_2O_3 nanosheets. The obtained 2D sheets exhibit a polycrystalline nature with a thickness of ≈2 nm. TEM with in situ heating reveals that upon thermal annealing at 250 °C for 2 h, the 2D oxide nanosheets showed slightly increased domain sizes, while the intergranular distorted regions were effectively removed. FETs were fabricated using annealed 2D In_2O_3 as the semiconducting channels, leading to a remarkable improvement in electron mobility when compared with un-annealed samples, and significantly surpassing the performance of devices based on many state-of-the-art 2D semiconductors. UV-detectors based on annealed 2D In_2O_3 also exhibited figures of merit that are an order of magnitude higher than those of devices made from freshly printed 2D In_2O_3. Overall, the 2D In_2O_3 nanosheets featured an excellent transparency – exceeding 99% – with a promising combination of electronic and optoelectronic features. These results confirm 2D In_2O_3 nanosheets derived from liquid metal are potential candidate for emerging transparent electronics applications such as invisible circuits, digital displays, smart contact lenses, and neural interfaces.

4. Experimental Section

Materials: Indium metal (In, 99.99%) was provided by Indium Corporation. Unless stated otherwise, all solvents were products from Sigma-Aldrich and used as received. 300 nm SiO_2/ p^+ Si wafers were purchased from D&X Co., Ltd.

Synthesis of 2D Indium Oxide Nanosheets: A set of 300 nm thick SiO_2/p^+ Si substrates were cleaned with acetone, propanol, and Mili-Q water, followed by blow-drying with compressed air. A squeeze printing technique was utilized to synthesize ultrathin In_2O_3 sheets by adapting previous reports.[5b,c] Prior to the synthesis, 300 nm SiO_2/Si substrates were preheated on a hot plate at 250 °C. An indium shot (0.3–0.5 g) was then placed and melted on a glass slide. As can be seen in Figure S8, Supporting Information, the molten indium metal appeared dull-gray due to the presence of a thick oxide layer with possible air-borne contaminants that formed during the storage of the precursor metal. Prior to the squeeze printing, this pre-existing oxide layer was removed by squeezing the molten metal with another glass slide. A small piece of liquid indium was then collected utilizing a glass pipette and transferred onto a desired substrate to perform the squeeze printing. The same method can also be applied to synthesize the material on glass and quartz substrates. A further cleaning process was conducted to remove metallic residues using Kapton sticky tape and solvent assisted cleaning described in previous studies.[5c] Prior to device fabrication, the obtained materials were annealed on a hotplate at a range of temperatures and durations. The synthesis and annealing processes were carried out in ambient air. As for the TEM samples, 2D In_2O_3 was directly printed onto the copper TEM grids via touch-printing.[19]

Characterizations of 2D In_2O_3 Nanosheets: All optical images were obtained using a Leica DM2500 optical microscope. The thickness of the 2D nanosheet and surface morphology were acquired with the aid of a Bruker Dimension Icon AFM operating under ScanAsyst-air mode. The collected data was then processed and analyzed with Gwyddion 2.55. TEM images were taken from a JEOL JEM-2100F TEM operating at an acceleration voltage of 200 kV equipped with a Gatan OneView camera. A Gatan 652 in situ heating holder was used to perform in-situ annealing. Gatan Microscopy suite software was utilized to analyze the data. XRD patterns were obtained using a Bruker D4 diffractometer with Cu Kα radiation (1.5418 Å). XPS spectra were obtained from a Thermo Scientific K-alpha XPS spectrometer with 1486.7 eV (Al Kα) X-ray source and concentric hemispherical electron analyzer. The XPS data were processed with CasaXPS software. UV–vis spectra and optical transmittance measurements were acquired from 2D In_2O_3 nanosheets prepared on quartz with a Cary 60 UV–vis spectrophotometer.

Device Fabrication and Measurement: The ultrathin In_2O_3-based field-effect transistors were fabricated via a photolithography process. First, the AZ 5214E photoresist was spin-coated on 2D In_2O_3 sheets deposited on 300 nm thick SiO_2/p^+ Si substrates prior to the electrode patterning using a Maskless Aligner – Heidelberg MLA150. An e-beam evaporator (PVD75 – Kurt J. Lesker) was then employed to deposit Cr/Au (10/100 nm) electrodes, followed by a lift-off process utilizing acetone to remove the photoresist residue. The FET measurements were performed using a probe station equipped with a Keysight B2902A Precision Source/Measure Unit (SMU). Variable-temperature measurements were conducted using a Linkam PE95 temperature controller equipped with a liquid nitrogen-cooled chamber. It is important to note that the electrode dimensions were assumed to be the length and width of the active channel and fringing currents might lead to a slightly overestimated carrier mobility. However, the determined values are sufficient to observe the effect of annealing on the overall electric properties of ultrathin indium oxide nanosheets. Optoelectronic measurements of two terminal devices were performed on a Linkam stage using a keysight B2912A source meter. The devices were illuminated using monochromatic LEDs from Thorlab (285 and 365 nm) at 0.4 mW cm^{-2} incident power and a bias voltage of 0.5 V. For cyclic repeatability measurements, an optical stimulus of 2000 s was used each cycle with a 4000 s recovery time before the next incoming pulse. All device performances were carried out at ambient conditions.

FET mobility was subsequently calculated by using the following equation[3d,5c,f]

$$\mu_e = \frac{L}{W}\frac{dI_{DS}}{dV_{GS}}\frac{1}{V_{DS}C_{ox}} \quad (1)$$

where μ_e refers to the electron mobility ($cm^2\ V^{-1}\ s^{-1}$), L is the channel length (20 µm) and W is the channel width (40 µm). I_{DS}, V_{DS}, V_{GS}, and C_{ox} represent the drain-source current and bias, the gate bias, and the gate insulator capacitance per unit area, respectively.

Photoresponsivity R (A W^{-1}), photodetectivity D^* (Jones), and external quantum efficiency EQE (%) were extracted from the photodetector performance by using the equations below[5c,20]

$$R = \frac{\Delta I_{ph}}{PS} \quad (2)$$

$$D^* = R\sqrt{\frac{S}{2eI_{dark}}} \quad (3)$$

$$EQE = \frac{hcR}{e\lambda} \times 100\% \quad (4)$$

where ΔI_{ph}, P, S, and I_{dark} are the change in photocurrent at incident illumination, power density, effective area subjected to illumination, and dark current. h, c, e, and λ represent Planck's constant, light speed, electron charge, and the wavelength of the incident light, respectively.

Supporting Information

Supporting Information is available from the Wiley Online Library or from the author.

Acknowledgements

The authors would also like to thank the RMIT Microscopy and Microanalysis Facility (RMMF) and the Micro Nano Research Facility (MNRF). N.S. recognizes the support of a McKenzie Postdoctoral Fellowship from the University of Melbourne. T.D., C.K.N., and P.A. acknowledge funding received from the Australian Research Council's (ARC) DECRA program (DE190100100). T.D. also acknowledges funding received from the ARC via the discovery program (DP220101923) and centre of excellence program (CE170100039). S.W. acknowledges funding support via ARC DP220100020. L.B. and X.T.W. acknowledge funding supports from ARC DECRA program (DE190101514).

Conflict of Interest

The authors declare no conflict of interest.

Data Availability Statement

The data that support the findings of this study are available in the Supporting Information of this article.

Keywords

2D, indium oxide, liquid metals, optoelectronics, thin film transistors (TFTs), transistors

Received: September 13, 2022
Revised: December 1, 2022
Published online: February 25, 2023

[1] a) C. Wang, R. Cheng, L. Liao, X. Duan, *Nano Today* **2013**, *8*, 514; b) Z. Lin, Y. Huang, X. Duan, *Nat. Electron.* **2019**, *2*, 378; c) A. Zavabeti, A. Jannat, L. Zhong, A. A. Haidry, Z. Yao, J. Z. Ou, *Nano-Micro Lett.* **2020**, *12*, 66; d) K. Kim, Y.-G. Park, B. G. Hyun, M. Choi, J.-U. Park, *Adv. Mater.* **2019**, *31*, 1804690.

[2] a) O. Bierwagen, *Semicond. Sci. Technol.* **2015**, *30*, 024001; b) C.-H. Huang, Y. Tang, T.-Y. Yang, Y.-L. Chueh, K. Nomura, *ACS Appl. Mater. Interfaces* **2021**, *13*, 52783; c) H. Frenzel, A. Lajn, M. Grundmann, *Phys. Status Solidi RRL* **2013**, *7*, 605; d) C. Glynn, C. O'Dwyer, *Adv. Mater. Interfaces* **2017**, *4*, 1600610; e) X. Yu, T. J. Marks, A. Facchetti, *Nat. Mater.* **2016**, *15*, 383; f) M. Si, Y. Hu, Z. Lin, X. Sun, A. Charnas, D. Zheng, X. Lyu, H. Wang, K. Cho, P. D. Ye, *Nano Lett.* **2021**, *21*, 500.

[3] a) P. Aukarasereenont, A. Goff, C. K. Nguyen, C. F. McConville, A. Elbourne, A. Zavabeti, T. Daeneke, *Chem. Soc. Rev.* **2022**, *51*, 1253; b) S. Zhao, J. Zhang, L. Fu, *Adv. Mater.* **2021**, *33*, 2005544; c) H. Xie, Z. Li, L. Cheng, A. A. Haidry, J. Tao, Y. Xu, K. Xu, J. Z. Ou, *iScience* **2022**, *25*, 103598; d) Y. Tang, C.-H. Huang, K. Nomura, *ACS Nano* **2022**, *16*, 3280.

[4] a) N. Cabrera, N. F. Mott, *Rep. Prog. Phys.* **1949**, *12*, 163; b) A. Zavabeti, J. Z. Ou, B. J. Carey, N. Syed, R. Orrell-Trigg, E. L. H. Mayes, C. Xu, O. Kavehei, A. P. O'Mullane, R. B. Kaner, K. Kalantar-zadeh, T. Daeneke, *Science* **2017**, *358*, 332.

[5] a) A. B. Hamlin, Y. Ye, J. E. Huddy, M. S. Rahman, W. J. Scheideler, *npj 2D Mater. Appl.* **2022**, *6*, 16; b) R. S. Datta, N. Syed, A. Zavabeti, A. Jannat, M. Mohiuddin, M. Rokunuzzaman, B. Y. Zhang, M. A. Rahman, P. Atkin, K. A. Messalea, M. B. Ghasemian, E. D. Gaspera, S. Bhattacharyya, M. S. Fuhrer, S. P. Russo, C. F. McConville, D. Esrafilzadeh, K. Kalantar-Zadeh, T. Daeneke, *Nat. Electron.* **2020**, *3*, 51; c) C. K. Nguyen, M. X. Low, A. Zavabeti, B. J. Murdoch, X. Guo, P. Aukarasereenont, A. Mazumder, A. Dubey, A. Jannat, M. A. Rahman, K. Chiang, V. K. Truong, L. Bao, C. F. McConville, S. Walia, T. Daeneke, N. Syed, *Adv. Opti. Mater.* **2022**, *10*, 2200925; d) Y. Ye, A. B. Hamlin, J. E. Huddy, M. S. Rahman, W. J. Scheideler, *Adv. Funct. Mater.* **2022**, *32*, 2204235; e) M. B. Ghasemian, A. Zavabeti, R. Abbasi, P. V. Kumar, N. Syed, Y. Yao, J. Tang, Y. Wang, A. Elbourne, J. Han, M. Mousavi, T. Daeneke, K. Kalantar-Zadeh, *J. Mater. Chem. A* **2020**, *8*, 19434; f) A. Jannat, N. Syed, K. Xu, M. A. Rahman, M. M. M. Talukder, K. A. Messalea, M. Mohiuddin, R. S. Datta, M. W. Khan, T. Alkathiri, B. J. Murdoch, S. Z. Reza, J. Li, T. Daeneke, A. Zavabeti, J. Z. Ou, *ACS Nano* **2021**, *15*, 4045.

[6] a) R. L. Weiher, *J. Appl. Phys.* **1962**, *33*, 2834; b) D. Dzhigaev, Y. Smirnov, P.-A. Repecaud, L. A. B. Marçal, G. Fevola, D. Sheyfer, Q. Jeangros, W. Cha, R. Harder, A. Mikkelsen, J. Wallentin, M. Morales-Masis, M. E. Stuckelberger, *Commun. Mater.* **2022**, *3*, 38.

[7] C. K. Nguyen, M. X. Low, A. Zavabeti, A. Jannat, B. J. Murdoch, E. D. Gaspera, R. Orrell-Trigg, S. Walia, A. Elbourne, V. K. Truong, C. F. McConville, N. Syed, T. Daeneke, *J. Mater. Chem. C* **2021**, *9*, 11815.

[8] Y. Magari, T. Kataoka, W. Yeh, M. Furuta, *Nat. Commun.* **2022**, *13*, 1078.

[9] X. Huang, C. Liu, S. Zeng, Z. Tang, S. Wang, X. Chen, D. W. Zhang, P. Zhou, *Adv. Mater.* **2021**, *33*, 2102201.

[10] G. Camino, S. M. Lomakin, M. Lazzari, *Polymer* **2001**, *42*, 2395.

[11] a) J. Wang, L. Ye, X. Wang, H. Zhang, L. Li, C. Kong, W. Li, *J. Alloys Compd.* **2019**, *803*, 9; b) C. Zhou, K. Liu, X. Chen, J. Feng, J. Yang, Z. Zhang, L. Liu, Y. Xia, D. Shen, *J. Alloys Compd.* **2020**, *840*, 155585.

[12] a) S. Wu, B. Son, L. Zhang, Q. Chen, H. Zhou, S. C. K. Goh, C. S. Tan, *J. Alloys Compd.* **2021**, *872*, 159696; b) D. Alagarasan, S. S. Hegde, S. Varadharajaperumal, K. D. Arun Kumar, R. Naik, S. P. Panjalingam, E. E. S. Massoud, R. Ganesan, *J. Mater. Sci.: Mater. Electron.* **2022**, *33*, 4794.

[13] M. Ouadhour, L. Derbali, S. Zargouni, M. Hajji, H. Ezzaouia, *J. Mater. Sci.: Mater. Electron.* **2018**, *29*, 8216.

[14] a) J. Xia, J. Yan, Z. X. Shen, *FlatChem* **2017**, *4*, 1; b) L. Jiao, W. Jie, Z. Yang, Y. Wang, Z. Chen, X. Zhang, W. Tang, Z. Wu, J. Hao, *J. Mater. Chem. C* **2019**, *7*, 2522.

[15] M. Marezio, *Acta Crystallogr.* **1966**, *20*, 723.

[16] S. Bae, H. Kim, Y. Lee, X. Xu, J.-S. Park, Y. Zheng, J. Balakrishnan, T. Lei, H. Ri Kim, Y. I. Song, Y.-J. Kim, K. S. Kim, B. Özyilmaz, J.-H. Ahn, B. H. Hong, S. Iijima, *Nat. Nanotechnol.* **2010**, *5*, 574.

[17] a) V. Senthilkumar, P. Vickraman, *Curr. Appl. Phys.* **2010**, *10*, 880; b) B. Pan, G. Yuan, X. Zhao, N. Han, Y. Huang, K. Feng, C. Cheng, J. Zhong, L. Zhang, Y. Wang, Y. Li, *Small Sci.* **2021**, *1*, 2100029.

[18] S. Husein, M. Stuckelberger, B. West, L. Ding, F. Dauzou, M. Morales-Masis, M. Duchamp, Z. Holman, M. I. Bertoni, *J. Appl. Phys.* **2018**, *123*, 245102.

[19] T. Daeneke, P. Atkin, R. Orrell-Trigg, A. Zavabeti, T. Ahmed, S. Walia, M. Liu, Y. Tachibana, M. Javaid, A. D. Greentree, S. P. Russo, R. B. Kaner, K. Kalantar-Zadeh, *ACS Nano* **2017**, *11*, 10974.

[20] a) M. X. Low, S. A. Tawfik, S. P. Russo, S. Sriram, M. Bhaskaran, S. Walia, *ACS Appl. Nano Mater.* **2022**, *5*, 12189; b) D. Kaur, M. Kumar, *Adv. Opt. Mater.* **2021**, *9*, 2002160.